Computational Materials Science 95 (2014) 328–336

Contents lists available at ScienceDirect

Computational Materials Science

journal homepage: www.elsevier.com/locate/commatsci

Optoelectronic and transport properties of Zintl phase $KBa_2Cd_2Sb_3$ compound

Saleem Ayaz Khan [a,*], A.H. Reshak [a,b,*]

[a] New Technologies – Research Center, University of West Bohemia, Univerzitni 8, 306 14 Pilsen, Czech Republic
[b] Center of Excellence Geopolymer and Green Technology, School of Material Engineering, University Malaysia Perlis, 01007 Kangar, Perlis, Malaysia

ARTICLE INFO

Article history:
Received 25 February 2014
Received in revised form 14 July 2014
Accepted 20 July 2014

Keywords:
Electronic structure
Optical properties
Thermoelectric properties
Seebeck coefficient

ABSTRACT

The electronic structure, optical response and transport properties of $KBa_2Cd_2Sb_3$ compound were calculated using the state-of-the-art all electron full potential linear augmented plane wave (FPLAPW) method. The calculated band structure and density of states exhibit an energy gap of about 0.71 eV. Close agreement was found among the optimized atomic positions, calculated bond lengths, bond angles and the experimental data. The bonding nature of $KBa_2Cd_2Sb_3$ was investigated using the calculated charge density contour plot. Additionally the complex dielectric function, refractive index, absorption coefficient, reflectivity and energy loss function were calculated and discussed in detail. The investigated optical parameters show high effectiveness for improvement of optoelectronic devices. The calculated uniaxial anisotropy value (0.01327) confirm there existence a considerable anisotropy among the spectral components of dielectric function and its derivatives. The investigation of electrical and thermal conductivities, Seebeck coefficient, power factor and figure of merit ($ZT = 1$) have confirmed that this material is a robust for thermoelectric applications.

1. Introduction

Energy crises are global problem and a big challenge of present time because of the reduction in fossil fuels with great consumption. On the other hand combustion of fossil fuels is major source of global pollution. Thermoelectric phenomena is the safe and fascinating way that deals with the conversion between thermal and electrical energy are expected to play an increasingly significant role to face the future energy challenges [1,2]. The complex bulk materials like clathrate, skutterudites and zintl phases were investigated to be highly efficient for thermoelectric properties [3–5].

Among them, the zintl phases that represent the important class of inter-metallic compounds are formed when early post-transition metals and semi-metals are combined with alkali and alkaline earth metals [6–8]. In this class of compounds the bonds formation are assumed to be occur by complete transfer of valence electrons depending on the electro-negativities of the atoms. According to this idea each atom is supposed to get a closed-shell state that confirms the octet rule, permitting the structure to be "broken down" to cations and (poly) anions [6–9]. Hence the zintl phases offer the bridging role between intermetallic and insulator compounds [10]. This class of compounds have attained considerable attention in the society of material engineering due to their diverse structures, and they are effective precursors for solution synthesis of nano-particles or metal clusters [9,11–16]. In recent years, zintl phase compounds have gained considerable attention as potential materials for thermoelectric applications [17,18]. In a sequence of latest articles [19–21], it has been shown that the desirable complex structures and electron transport properties of the zintl phases can lead to enhanced thermoelectric performance.

An imperative work has been done on expanding the chemistry of the zintl phases towards the transition metals (half and filled d-states), and the metals from the lanthanide series. The Saprov et al. [10] synthesized and structurally characterized many novel ternary compounds, where $Sr_9Cd_{4+x}Sb_9$ and $Ca_9Zn_{4+x}Sb_9$ [22,23], $Eu_{11}Cd_6Sb_{12}$ and $Eu_{11}Zn_6Sb_{12}$ [24], $Ba_{21}Cd_4Bi_{18}$ and $Ba_{21}Cd_4Sb_{18}$ [25], $Ba_3Cd_2Sb_4$ [26], Yb_2CdSb_2 [27], are few examples with the divalent alkaline-earth and rare-earth metals. Saprov et al. [10] also synthesized five new zintl phases $KA_2Cd_2Sb_3$ (A = Ca, Sr, Ba, Eu, Yb) compounds. They have used tight-binding linear muffin-tin orbital (TB-LMTO) method with LDA (Von Barth and Hedin) [28] to calculate the electronic band structure. Generally LDA underestimate the calculated energy gap in comparison to experimental data. Moreover it is impossible to develop photonic devices for optical communication without proper understanding of

* Corresponding authors. Tel.: +420 777 083 956 (S.A. Khan), tel.: +420 777 729 583 (A.H. Reshak).
E-mail addresses: sayaz_usb@yahoo.com (S.A. Khan), maalidph@yahoo.co.uk (A.H. Reshak).

http://dx.doi.org/10.1016/j.commatsci.2014.07.031
0927-0256/

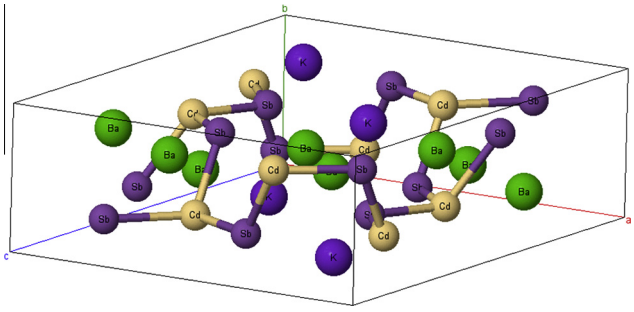

Fig. 1. Optimize unit cell of $KBa_2Cd_2Sb_3$ semiconductor.

Table 1
Present optimized and experimental cryptographic data of $KBa_2Cd_2Sb_3$ semiconductor.

Atom	*X* (opt.)[a]	Expt.	*Y* (opt.)[a]	(Expt.)	*Z* (opt.)[a]	Expt.
K	0.39941	0.39950	1/4	1/4	0.55417	0.55420
Ba1	0.09913	0.09900	1/4	1/4	0.42773	0.42739
Ba2	0.37277	0.37313	1/4	1/4	0.28959	0.28929
Cd1	0.30499	0.30416	1/4	1/4	0.08358	0.08380
Cd2	0.36456	0.36477	1/4	1/4	0.78340	0.78276
Sb1	0.07942	0.07932	1/4	1/4	0.63495	0.63407
Sb2	0.13443	0.13491	1/4	1/4	0.19620	0.19685
Sb3	0.71219	0.71313	1/4	1/4	0.57554	0.57575

Exp. [10].
[a] Present work with GGA-PBE.

optical properties of the materials [29]. The optical properties give deep insight into material's structure therefore it is necessary to highlight the optical properties of the investigated compound.

Present work is aimed in calculating the structural, electronic, optical and thermoelectric properties of $KBa_2Cd_2Sb_3$ compound using the full potential linear augmented plane wave (FP-LAPW) method which confirmed to be one of the most precise method [30,31] within a framework of density functional theory (DFT).

2. Crystal structure and computational detail

The structure of $KBa_2Cd_2Sb_3$ was crystallized in orthorhombic symmetry having space group Pnma (No. 62) with four molecules per unit cell [10]. The optimized crystal structure of $KBa_2Cd_2Sb_3$ compound is represented in Fig. 1. The optimized atomic positions along with the experimental data [10] are listed in Table 1. The present calculations are performed using the full potential linear augmented plane wave (FPLAPW) method within the frame work of WIEN2K code [32]. The self-consistent calculations were achieved by using local density approximation (LDA-CA) [33], generalized gradient approximation (GGA-PBE) [34], and Engel Vosko generalized gradient approximation (EVGGA) [35]. In order to converge the energy eigenvalues the wave function in the interstitial region was expanded in plane waves with cutoff $R_{MT}K_{max} = 7.0$. Where R_{MT} represent the muffin-tin (MT) sphere radius and K_{max} corresponds to the magnitude of largest K vector in plane wave expansion. The selected MT sphere radii (R_{MT}) are 2.0 a.u. for K, Ba, Cd and Sb, respectively. The wave function inside the sphere was expanded up to $l_{max} = 10$ where as the Fourier expansion of the charge density was up to $G_{max} = 12(\text{a.u.})^{-1}$. The crystal structure is optimized by minimization of forces acting on the atoms. The convergence of the self-consistent calculations are considered to be converged when the difference in total energy of the crystal did not exceed 10^{-2} mRyd and the forces are less than 1 mRyd/a.u. for successive steps. The self consistencies were obtained by 120 k points in irreducible Brillouin zone (IBZ), initiated from 1000 k points in the Brillouin zone (BZ).

3. Results and discussion

3.1. Band structure and density of state

The calculated electronic band structure plays a significant role in understanding the nature of the materials. The electronic band structure of $KBa_2Cd_2Sb_3$ was calculated along high symmetry point using three schemes LDA-CA, GGA-PBE and EV-GGA as shown in Fig. 2(a–c). The calculated band structures show that the valence band maximum (VBM) and conduction band minimum (CBM) are located at the centre of BZ resulting a direct band gap ($\Gamma \rightarrow \Gamma$). The calculated values of the energy gap using three schemes are 0.26 eV (LDA), 0.37 eV (GGA) and 0.71 eV (EVGGA). Generally LDA-CA and GGA-PBE underestimate the value of the calculated energy band gap in comparison to the experimental one. This is mainly due to the fact that they have simple forms that are not sufficiently flexible to accurately reproduce both the exchange–

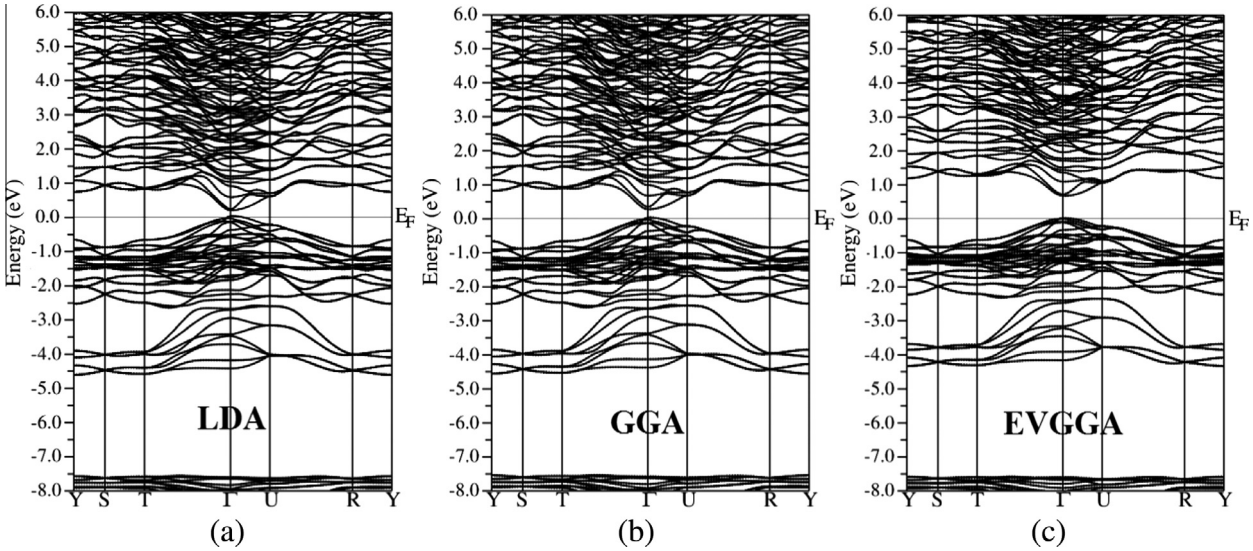

Fig. 2. Calculated band structure of $KBa_2Cd_2Sb_3$ semiconductor; (a) LDA; (b) GGA; (c) EVGGA.

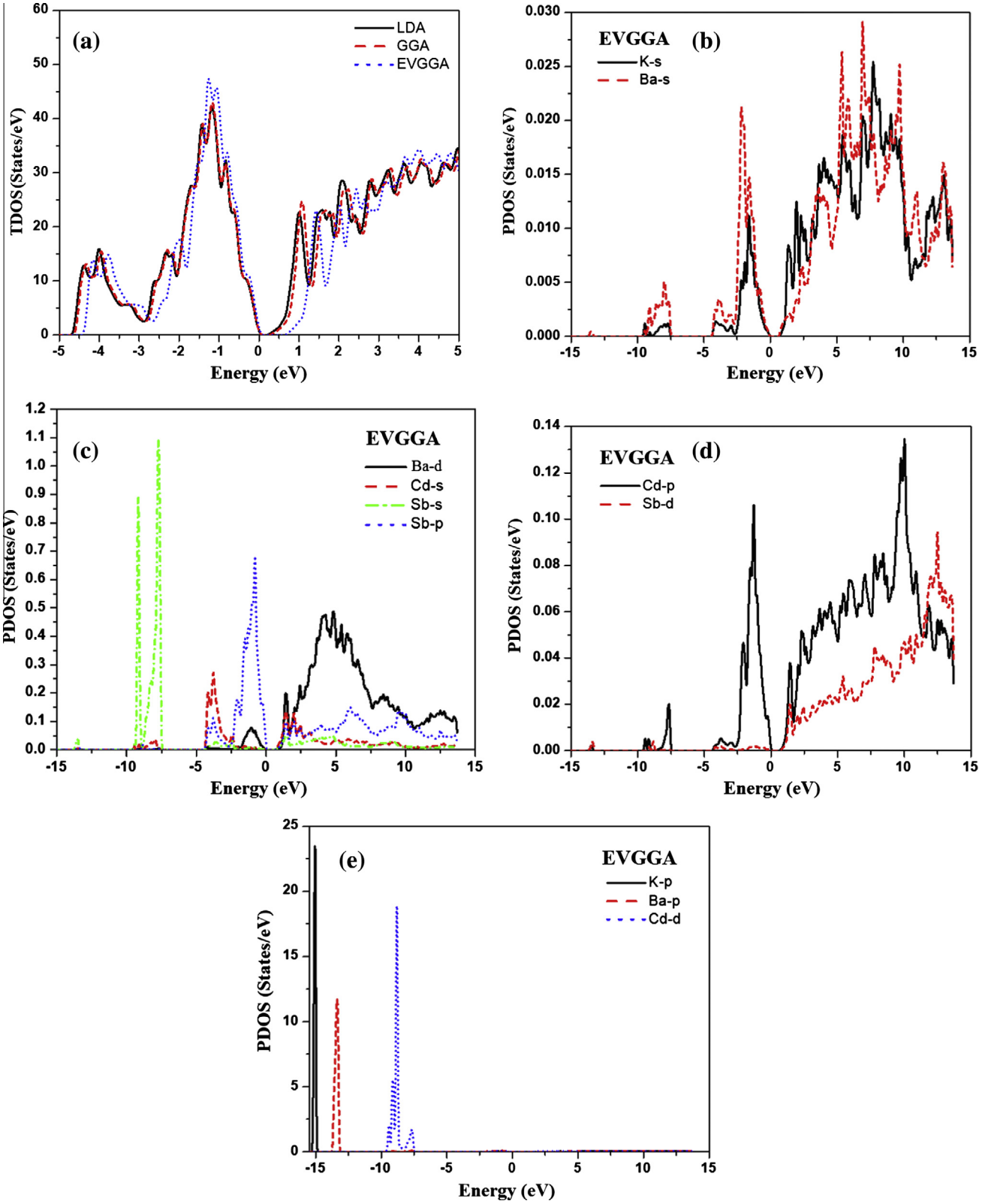

Fig. 3. Calculated total and partial densities of states (states/eV unit cell); (a) TDOS using LDA, GGA, EVGGA; (b–e) PDOS using EVGGA.

correlation energy and its charge derivative. Usually EVGGA was obtained by optimizing the exchange–correlation potential V_{xc} instead of the corresponding energy E_{xc}. This approach yields better band splitting and structural properties that mainly depend on the accuracy of the exchange–correlation potential [36–38] therefore this functional is selected for further explanation of partial density of states (PDOS).

The calculated total and partial density of states are shown in Fig. 3(a–e). The calculated partial density of states (PDOS) show that the core bands around −15.0 eV is formed by K-p state. The

peak around −13.6 eV is shaped by Sb-s/d, Ba-s/p and Cd-p states. In energy range from −9.8 to −7.5 eV, the bands are originated from prevailing Cd-d state with negligible contribution of Ba-s, K-s, Cd-s/p and Sb-s/p/d states. In the energy range between −4.2 and −2.5 eV the bands are mostly formed with foremost Cd-s and Sb-p states while the contribution of the other states is very small. The lower and upper valence bands are formed by predominant Cd-d and Sb-p states with small contribution from K-s, Ba-s, and Sb-d states. The conduction band is mainly shaped by Cd-s and Sb-p states with small part of Cd-p and Sb-s/d states. The higher energy bands are shaped by Cd-s/p and Sb-p with small contribution from K-s, Ba-s/d and Sb-s/d states.

3.2. Electronic charge density

The precise bonds nature of the materials can be justify by electronic charge density plot [39,40]. To envisage the chemical bonding nature among the composition of $KBa_2Cd_2Sb_3$ compound, we have calculated the distribution of charge density in the (030) crystallographic plane as shown in Fig. 4. The thermo-scale shows the intensity of the charge density, in which the blue[1] color represent the maximum intensity while the red color exhibit the zero charge density. The spectra of the electronic charge density show there exists a strong ionic bonding between Cd and Sb, also partially covalent and dominant ionic bonds between Sb and Ba atoms. Further study confirm that inter atomic distance between Cd–Sb is less than that of Ba–Sb indicating the strength of Cd–Sb bonds. From the calculated electronic charge density it is clear that the charge density around the Sb atom is maximum than the other atoms. We have also calculated bond lengths and angles which show good agreement with experimental data [10]. These are listed in Tables 2 and 3.

3.3. Optical properties

The complex dielectric function $\varepsilon(\omega)$ is directly related to the energy band structure of solids. The optical spectroscopy analysis of $\varepsilon(\omega)$ is a powerful tool to determine the overall band behavior of a solid. The present work deals with complex dielectric function $\varepsilon(\omega) = \varepsilon_1(\omega) + i\varepsilon_2(\omega)$ which is the most important aspect for calculating the optical response of the material. The dielectric function's dispersions contain intra- and inter-band transitions. The intra-band transitions are important only for metals. Inter-band transitions are further divided into direct and indirect band transitions. We ignore the phonons contribution involved in the indirect inter-band transition and only consider direct band transition between occupied and unoccupied states. For the calculation of frequency dependent dielectric function $\varepsilon(\omega)$, we need to have the correct energy eigenvalues and electron wave functions [41]. Both energy eigenvalues and electron wave functions are the natural output of calculating the band structure. The crystal structure symmetry of $KBa_2Cd_2Sb_3$ allowed only three principal diagonal non-zero second order dielectric tensor components. These are $\varepsilon^{xx}(\omega)$, $\varepsilon^{yy}(\omega)$ and $\varepsilon^{zz}(\omega)$ along **a**, **b** and **c** crystallographic axis. These dielectric tensor components of $\varepsilon_2(\omega)$ are required for complete description of linear optical susceptibilities. These components can be obtained using the expression taken from Ref. [42].

$$\varepsilon_2^{ij} = \frac{4\pi^2 e^2}{Vm^2\omega^2} \times \sum_{nn'\sigma} \langle kn\sigma|p_i|kn'\sigma\rangle\langle kn'\sigma|p_j|kn\sigma\rangle \times f_{kn}(1 - f_{kn'})\delta(E_{kn'} - E_{kn} - \hbar\omega) \quad (1)$$

In this expression m and e stand for mass and charge of electron and ω represent the electromagnetic radiation striking the crystal, V represent the volume of the unit cell, in bracket notation p correspond to momentum operator, $|kn\sigma\rangle$ represent the crystal wave function with crystal momentum k, and σ spin correspond to the eigenvalue E_{kn}. The Fermi distribution function correspond to f_{kn} which makes sure the counting of transition from occupied to unoccupied state. The term $\delta(E_{kn'} - E_{kn} - \hbar\omega)$ shows the condition for conservation of total energy. The spectral peaks of absorptive part of dielectric function exhibit the allowed electric-dipole transitions between the valence and conduction bands. In order to identify these structures we need to look at the magnitude of the optical matrix elements. The observed structures would correspond to those transitions that have large optical matrix dipole transition elements.

[1] For interpretation of color in Fig. 4, the reader is referred to the web version of this article.

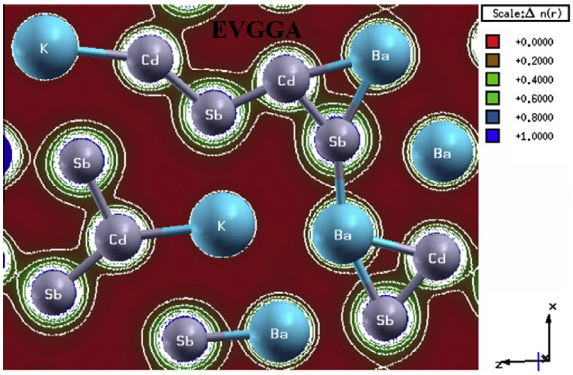

Fig. 4. Electronic charge density contour of $KBa_2Cd_2Sb_3$ in (030) plane.

Table 2
Calculated bond length of $KBa_2Cd_2Sb_3$ single molecule.

Bonds (Å)	Present work[a]	Expt.
Sb1–Cd1 × 2	3.023	3.023
Sb1–Cd2	3.133	3.140
Sb2–Cd2 × 2	2.868	2.856
Sb2–Cd1	2.925	2.916
Sb3–Cd1	2.926	2.923
Sb3–Cd2	3.092	3.091
Cd1–Sb2	2.925	2.916
K–Sb2 × 2	3.455	3.446
K–Sb3 × 2	3.598	3.606
Ba1–Sb1	3.474	3.465
Ba1–Sb3 × 2	3.497	3.489
Ba1–Sb1 × 2	3.562	3.553
Ba2–Sb2	3.443	3.443
Ba2–Sb3 × 2	3.525	3.531
Ba2–Sb1 × 2	3.630	3.636

Expt. [10].
[a] Present work with GGA-PBE.

Table 3
Calculated bond angles of $KBa_2Cd_2Sb_3$ single molecule.

Angles (°)	Present work[a]	Expt.
Sb2–Cd2–Sb1	102.55	102.78
Sb3–Cd2–Sb1	104.47	103.79
Sb2–Cd1–Sb3	105.47	106.27
Sb1–Cd1–Sb1	109.57	109.51
Sb3–Cd1–Sb1	117.85	117.41
Sb2–Cd2–Sb2	118.88	119.63

Expt. [10].
[a] Present work with GGA-PBE.

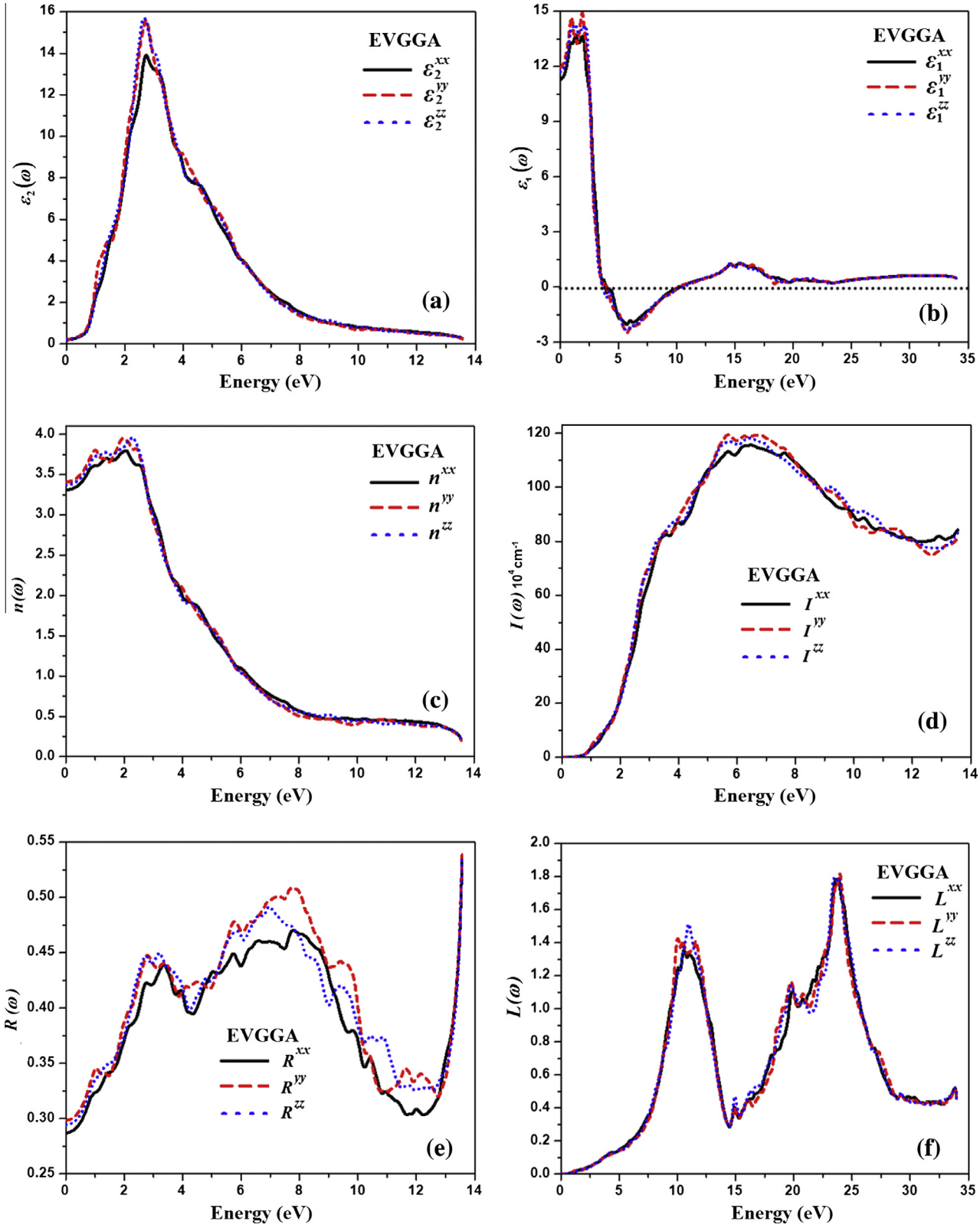

Fig. 5. (a) Calculated $\varepsilon_2^{xx}(\omega)$, $\varepsilon_2^{yy}(\omega)$ and $\varepsilon_2^{zz}(\omega)$ (b) calculated $\varepsilon_1^{xx}(\omega)$, $\varepsilon_1^{yy}(\omega)$ and $\varepsilon_1^{zz}(\omega)$ (c) calculated $n^{xx}(\omega)$, $n^{yy}(\omega)$ and $n^{zz}(\omega)$ (d) calculated $I^{xx}(\omega)$, $I^{yy}(\omega)$ and $I^{zz}(\omega)$ (e) calculated $R^{xx}(\omega)$, $R^{yy}(\omega)$ and $R^{zz}(\omega)$ (f) calculated $L^{xx}(\omega)$, $L^{yy}(\omega)$ and $L^{zz}(\omega)$.

Fig. 5(a) represents the absorptive (imaginary) optical spectra of dielectric tensor components. Broadening is taken to be 0.1 eV which is typical of the experimental accuracy. The narrow band gap semiconductor $KBa_2Cd_2Sb_3$ shows transparency to the electromagnetic (EM) waves in lower energy region. The fundamental absorption edge occurs at 0.71 eV for $\varepsilon_2^{xx}(\omega)$, $\varepsilon_2^{yy}(\omega)$ and $\varepsilon_2^{zz}(\omega)$, respectively. These fundamental absorption edges provide information about threshold for direct optical transitions between the valence and conduction band extrema's. The dominant peaks in spectral components of $\varepsilon_2(\omega)$ are positioned around 2.7 eV

corresponds to the transition of electrons which arise mainly from direct transition from occupied to unoccupied bands. The real part of the frequency dependent dielectric function is related to the electric polarizability of the material and can be calculated from imaginary part using Kramers–Kronig relation [43].

$$\varepsilon_1(\omega) = 1 + \frac{2}{\pi} P \int_0^{\infty} \frac{\omega' \varepsilon_2(\omega')}{\omega'^2 - \omega^2} d\omega' \quad (2)$$

In the given expression P symbolize the principal value of integral. Fig. 5(b) shows the calculated real part of the frequency dependent dielectric function $\varepsilon_1(\omega)$. In energy range from (0–2.5 eV) and (3.5–7.5 eV) there is anisotropy among $\varepsilon_1^{xx}(\omega)$, $\varepsilon_1^{yy}(\omega)$ and $\varepsilon_1^{zz}(\omega)$. The rest of range shows isotropy among the three components. The calculated optical dielectric constants at zero energy $\varepsilon_1^{xx}(\omega)$, $\varepsilon_1^{yy}(\omega)$ and $\varepsilon_1^{zz}(\omega)$ are 10.9, 11.6 and 11.4 eV, respectively. The maximum peaks are located at 1.3 eV for $\varepsilon_1^{xx}(\omega)$, 1.9 eV for $\varepsilon_1^{yy}(\omega)$ and 1.6 eV for $\varepsilon_1^{zz}(\omega)$, respectively. The calculated uniaxial anisotropy $\delta\varepsilon = [(\varepsilon_0^{\parallel} - \varepsilon_0^{\perp})/\varepsilon_0^{tot}]$ is 0.01327, indicating the considerable anisotropy [44] among the spectral components of the dielectric function.

Fig. 5(b) also elucidates that at very low frequencies the optical properties of $KBa_2Cd_2Sb_3$ reveal a metal-like characteristics, whereas at highest frequencies the optical spectra behave like insulators. A distinctive frequency at which the material changes from a metallic to a dielectric response is called the plasma frequency ω_p which is defined as the frequency at which the real part of the dielectric function vanishes $\varepsilon_1(\omega) = 0$ [45]. The calculated values of ω_p^{xx}, ω_p^{yy} and ω_p^{zz} are shown in Table 4.

The other optical properties such as refractive index $n(\omega)$, reflectivity $R(\omega)$, absorption coefficient $I(\omega)$, and energy loss function $L(\omega)$ can be evaluated using the calculated spectra of $\varepsilon_1(\omega)$ and $\varepsilon_2(\omega)$ as shown in Fig. 5(c–f). The calculated static values of non-zero tensor components of refractive index and real part of dielectric tensor components are shown in Table 4. We note that a smaller energy gap yields a larger $\varepsilon_1(0)$ value. This could be explained on the basis of the Penn model [46].

$$\varepsilon_1(0) \approx 1 + (\hbar\omega_P/E_g)^2 \quad (3)$$

E_g is some kind of averaged energy gap which could be related to the real energy gap and ω_P represent plasma frequency. It is obvious that $\varepsilon_1(0)$ is inversely proportional to E_g. Hence a large E_g yields a smaller $\varepsilon_1(0)$. Also $\varepsilon_1(0)$ is directly related to the $n(0)$ by the relation $n(0) = \sqrt{\varepsilon_1(0)}$. The three non-zero components of $R(\omega)$ show 28.8, 29.4 and 29.8% reflection at 0.0 eV. The reflectivity spectra shows considerable anisotropy among the three components in the energy range between 0.0 and 12.8 eV and shows isotropy in higher energy range (12.8–13.5 eV). The maximum reflectivity (59%) is found at higher energies.

The calculated absorption coefficient $I(\omega)$ corresponding to the band gap of the material, show short cut-off in IR region increases from 0.71 eV and shows maximum absorption of $115 \times 10^4\ cm^{-1}$ (6.5 eV), $119 \times 10^4\ cm^{-1}$ (5.5 eV) and $118 \times 10^4\ cm^{-1}$ (6.5 eV). The spectral components show weak isotropy up to 2.8 eV. For rest of range there is considerable anisotropy among $I^{xx}(\omega)$, $I^{yy}(\omega)$ and $I^{zz}(\omega)$.

The $L(\omega)$ describes the energy loss by fast moving electron inside the material. The sharp peaks produced in $L(\omega)$ around 10.5, 10.0 and 11.0 eV are due to the plasma oscillation [47]. The above cases show considerable anisotropy among the three tensor components in the energy range (10–12.5) eV and (15–23) eV while rest of range shows isotropic behavior among the three components.

Table 4
Calculated band gap and other optical constants of $KBa_2Cd_2Sb_3$ single crystal.

	LDA	GGA	EVGGA
$\varepsilon_1^{average}(0)$	16.4	15.0	11.3
$\varepsilon_1^{xx}(0)$	15.8	14.5	10.9
$\varepsilon_1^{yy}(0)$	17.0	15.5	11.6
$\varepsilon_1^{zz}(0)$	16.3	15.0	11.4
$n^{xx}(0)$	3.98	3.81	3.31
$n^{yy}(0)$	4.13	3.94	3.40
$n^{zz}(0)$	4.04	3.87	3.37
E_g (eV)	0.26	0.37	0.71
ω_p^{xx}	0.05	0.03	0.01
ω_p^{yy}	0.44	0.40	0.25
ω_p^{zz}	0.04	0.05	0.05

3.4. Thermoelectric properties

Thermoelectric materials are prominent group of compounds which keep importance in both traditional research and industrial side. The thermoelectric devices are often more reliable than traditional mechanical devices and suffer less wear. On the other hand, efficiency of the thermoelectric devices is much less than traditional devices. In order to increase the efficiency of these devices, we need to investigate materials with enhanced thermoelectric properties [48]. Using the calculated band structure, one can evaluate the thermoelectric transport tensors using the standard Boltzmann kinetic transport theory and the rigid band approach [49]. The main factors for discussing the thermoelectric properties are electrical conductivity, Seebeck coefficient tensors and thermal conductivity which are the function of temperature (T) and chemical potential (μ) expressed in Refs. [49,50].

The BoltzTrap program [49] is used for calculating the transport properties which depend on a well tested smoothed Fourier interpolation to obtain an analytical expression of bands. In the present approach the relaxation time τ is taken to be a constant because it cannot be determined from band structure calculations. On the basis of consequence that the electrons participate to transport are in a narrow energy range due to the delta-function like Fermi broadening. For such a narrow energy range the relaxation time is nearly the same for the electrons. The validity of this method has been tested earlier which turns out to be a good approximation [51]. The dependence of temperature for energy band structure is ignored.

It is proven that high thermoelectric efficiency is the result of high electrical conductivity, large Seebeck coefficient and low thermal conductivity [17]. The thermoelectric performance of a material is characterized by the dimensionless figure of merit (ZT).

$$ZT = \frac{S^2 T \sigma}{(k_{el} + k_{ph})} \quad (4)$$

where S represents the Seebeck coefficient, σ is the electrical conductivity, and k_{el}, k_{ph} are the thermal conductivities attributed to electrons and phonons, respectively.

Fig. 6(a–e) demonstrates average values of tensor components of transport properties vs. chemical potential (μ) at 300, 500 and 700 K. The average electrical conductivity $(\sigma/\tau)^{av}$ represents higher value of $5.6 \times 10^{19}(\Omega\,m\,s)^{-1}$ and $4.7 \times 10^{19}(\Omega\,m\,s)^{-1}$ for n-type and p-type regions at 300 K. When temperature is increased to 500 K and 700 K the lattice thermal conductivity shifts the electrons to the conduction band and material show metallic behaviors. The collision of the electron in the conduction band resists the mobility of electron and as a result the $(\sigma/\tau)^{av}$ in both n- and p-type region decreased as shown in Fig. 6(a).

The magnitude and sign of the Seebeck coefficient is linked to the asymmetry of the electron distribution around the Fermi level [52]. The selected Fermi energy creates an asymmetric energy distribution of electrons moving in the material concerning the Fermi

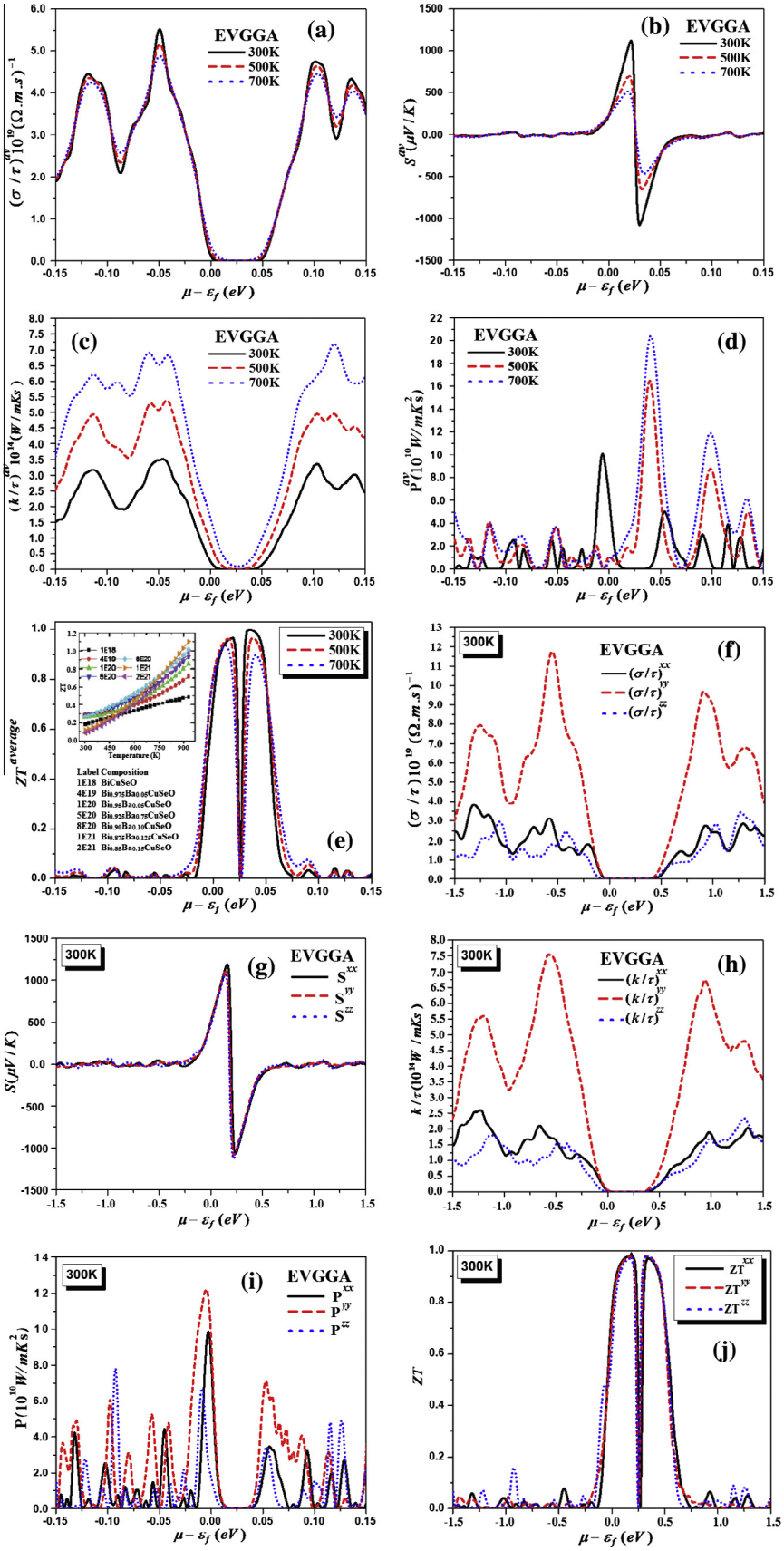

Fig. 6. (a) Calculated $(\sigma/\tau)^{av}$ (b) calculated S^{av} (c) calculated $(k/\tau)^{av}$ (d) calculated P^{av} (e) calculated ZT^{av} (f) calculated $(\sigma/\tau)^{xx}$, $(\sigma/\tau)^{yy}$ and $(\sigma/\tau)^{zz}$ (g) calculated S^{xx}, S^{yy} and S^{zz} (h) calculated $(k/\tau)^{xx}$, $(k/\tau)^{yy}$ and $(k/\tau)^{zz}$ (i) calculated P^{xx}, P^{yy} and P^{zz} (j) calculated ZT^{xx}, ZT^{yy} and ZT^{zz}.

energy results a greater value of Seebeck coefficient. In contrast reduction in the Joule heating results decrease in conductivity agrees with the reported work of Vashaee and Shakouri [53]. The Seebeck coefficient (S^{av}) shows maximum value of 1150 μV/K and −1100 μV/K at 300 K. As one move towards higher temperature (500 K and 700 K) the S^{av} reduced to ±700 μV/K and ±500 μV/K as shown in Fig. 6(b).

The phonon subsystem also gives crucial contribution [54] but in the present calculation the BoltzTraP code calculates only the electronic thermal conductivity. The average thermal conductivity $(k/\tau)^{av}$ shows the converse result elucidate less value (3.5×10^{14} W/m K s and 3.25×10^{14} W/m K s) for n and p-type at 300 K. At 500 K, $(k/\tau)^{av}$ increased to 5.25×10^{14} and 4.90×10^{14} W/m K s. When temperature is increased to 700 K, the energy barrier become thin as shown in Fig. 6(c) and $(k/\tau)^{av}$ further increased to 6.9×10^{14} W/m K s and 7.0×10^{14} W/m K s in n- and p-type region, respectively.

The most important quantity for measuring transport properties is power factor (P). The calculated values of power factor ($P^{av} = S^2\sigma/\tau$) for $KBa_2Cd_2Sb_3$ are shown in Fig. 6(d). At 300 K, the calculated P^{av} show maximum value of 10.0×10^{10} W/mK^2 s in n-type region near the energy barrier. When temperature is increased to 500 K, the spectral peak of P^{av} shifts to p-type region and shows maximum value of 16.4×10^{10} W/mK^2 s. At 700 K, P^{av} has increased to 20.5×10^{10} W/mK^2 s in p-type region.

The most important quantity for measuring transport properties is figure of merit (ZT) as shown in Fig. 6(e). The calculated value of dimensionless ZT^{av} also shows significant value (0.95 for p type and 1.0 for n-type) at 300 K. The calculated ZT^{av} are compared to the experimental figure of Li et al. [55] as shown in Fig. 6(e) which highlight the importance of the $KBa_2Cd_2Sb_3$ for thermoelectric applications.

The ZT^{av} show significant result at 300 K therefore we selected this temperature (300 K) for further explanation of anisotropic character of transport properties.

The three principal dielectric tensor components of σ/τ, S, k/τ and P and ZT are shown in Fig. 6(f–j). The three principal tensor components of electrical conductivity are $(\sigma/\tau)^{xx}$, $(\sigma/\tau)^{yy}$ and $(\sigma/\tau)^{zz}$ which show considerable anisotropy. It is observed that $(\sigma/\tau)^{yy}$ is more dominant having the value of $2.65 \times 10^{14}(\Omega\,\mathrm{m\,s})^{-1}$ and $9.6 \times 10^{19}(\Omega\,\mathrm{m\,s})^{-1}$ in n-type and p-type region, respectively. The contribution of $(\sigma/\tau)^{xx}$ is small having value of 3.9×10^{14} $(\Omega\,\mathrm{m\,s})^{-1}$ in n-type region which reduced to $2.7 \times 10^{14}(\Omega\,\mathrm{m\,s})^{-1}$ in p-type region. The component $(\sigma/\tau)^{zz}$ shows small contribution $(3.0 \times 10^{14}(\Omega\,\mathrm{m\,s})^{-1})$ in n-type region. It shifts towards higher value $(3.4 \times 10^{14}(\Omega\,\mathrm{m\,s})^{-1})$ in p-type region. Moreover the three components S^{xx}, S^{yy} and S^{zz} shows considerable anisotropy except in the range between −0.1 and 0.6 eV which shows isotropic behavior among the three components. The thermal conductivity spectra also shows considerable anisotropy among $(k/\tau)^{xx}$, $(k/\tau)^{yy}$ and $(k/\tau)^{zz}$. The component $(k/\tau)^{yy}$ is foremost in whole range. The three components P^{xx}, P^{yy} and P^{zz} also show considerable anisotropy. The P^{yy} component is more dominant around 0.0 eV and show maximum value of 12.1×10^{10} W/mK^2 s. It reduced to 10×10^{10} W/mK^2 s for p^{xx} while p^{yy} show maximum peak (12.1×10^{10} W/mK^2 s) in n-type region (−0.08 eV).

The three components ZT^{xx}, ZT^{yy} and ZT^{zz} show isotropic behavior from −0.05 to 0.6 eV while rest of the range show considerable anisotropy.

4. Conclusion

All electron full potential linear augmented plane wave (FPLAPW) method based on DFT was used for calculating the electronic structure, valence electron charge density and linear optical properties of $KBa_2Cd_2Sb_3$ semiconductor. The exchange correlation energy was solved with three schemes namely; local density approximation (LDA-CA), generalized gradient approximation (GGA-PBE) and Engel Vosko generalized gradient approximation (EVGGA). We have explored the band structure and density of states of the reported compound which has validated that EVGGA give better energy gap value (0.71 eV). The electronic charge density contour visualized bonding nature of the constituent atoms. Moreover the optical spectra of dielectric tensor components of imaginary $\varepsilon_2(\omega)$ and real part $\varepsilon_1(\omega)$ were calculated. Based on calculated uniaxial anisotropy value (0.01327) we have concluded that there is considerable anisotropy among the spectral components of $KBa_2Cd_2Sb_3$. The other optical constants such as refractive index $n(\omega)$, absorption coefficient $I(\omega)$, reflectivity $R(\omega)$ and energy loss function $L(\omega)$ were calculated using $\varepsilon_1(\omega)$ and $\varepsilon_2(\omega)$ which show high suitability for practical application of optoelectronic devices. Moreover the electrical conductivity, thermal conductivity, seebeck coefficient and figure of merit were discussed in detail. The analysis of figure of merit and power factor confirmed that $KBa_2Cd_2Sb_3$ is good thermoelectric material suitable for technological applications.

Acknowledgments

The result was developed within the CENTEM project, reg. no. CZ.1.05/2.1.00/03.0088, co-funded by the ERDF as part of the Ministry of Education, Youth and Sports OP RDI program. MetaCentrum and the CERIT-SC under the program Centre CERIT Scientific Cloud, reg. no. CZ.1.05/3.2.00/08.0144.

References

[1] M.S. Dresselhaus, Gang Chen, Ming Y. Tang, Ronggui Yang, Hohyun Lee, Dezhi Wang, Zhifeng Ren, Jean-Pierre Fleurial, Pawan Gogna, Adv. Mater. 19 (2007) 1043–1053.
[2] G. Jeffrey, Snyder1 & Eric S Toberer, Nat. Mater. 7 (2008) 105–114.
[3] G.S. Nolas, J. Poon, M. Kanatzidis, Mater. Res. Soc. Bull. 31 (2006) 199–205.
[4] C. Uher, in: T. Tritt (Ed.), Thermoelectric Materials Research I, Semiconductors and Semimetals Series 69, Elsevier, 2001, pp. 139–253.
[5] S.M. Kauzlarich, S.R. Brown, G.J. Snyder, Dalton Trans. (2007) 2099–2107.
[6] E. Zintl, Angew. Chem. 52 (1939) 1–6.
[7] R. Nesper, Prog. Solid State Chem. 20 (1990) 1–45.
[8] S.M. Kauzlarich (Ed.), Chemistry, Structure, and Bonding of Zintl Phases and Ions, VCH Publishers, New York, 1996.
[9] J.D. Corbett, Angew. Chem., Int. Ed. 39 (2000) 670–690.
[10] B. Saprov, M. Broda, K.V. Ramanujachary, S. Bobev, Polyhedron 29 (2010) 456–462.
[11] J.D. Corbett, Chem. Rev. 85 (1985) 383–393.
[12] Z. Downie, A.M. Tang, Guloy, Angew. Chem., Int. Ed. 39 (2000) 337–340.
[13] T.F. Faessler, Coord. Chem. Rev. 215 (2001). 377-377.
[14] B. Kesanli, J. Fettinger, D.R. Gardner, B. Eichhorn, J. Am. Chem. Soc. 124 (2002) 4779–4786.
[15] S.C. Sevov, J.M. Goicoechea, Organometallics 25 (2006) 5678–5692.
[16] D. Sun, A.E. Riley, A.J. Cadby, E.K. Richman, S.D. Korlann, S.H. Tolbert, Nature 441 (2006) 1126–1130.
[17] G.J. Snyder, E.S. Toberer, Nat. Mater. 7 (2008) 105–114.
[18] S.M. Kauzlarich, S.R. Brown, G.J. Snyder, Dalton Trans. 21 (2007) 2099–2107.
[19] S.R. Brown, S.M. Kauzlarich, F. Gascoin, G.J. Snyder, Chem. Mater. 18 (2006) 1873–1877.
[20] E.S. Toberer, C.A. Cox, S.R. Brown, T. Ikeda, A.F. May, S.M. Kauzlarich, G.J. Snyder, Adv. Funct. Mater. 18 (2008) 2795–2800.
[21] F. Gascoin, S. Ottensmann, D. Stark, S.M. Haile, G.J. Snyder, Adv. Funct. Mater. 15 (2005) 1860–1864.
[22] S. Bobev, J.D. Thompson, J.L. Sarrao, M.M. Olmstead, H. Hope, S.M. Kauzlarich, Inorg. Chem. 43 (2004) 5044–5052.
[23] S.Q. Xia, S. Bobev, J. Am. Chem. Soc. 129 (2007) 10011–10018.
[24] B. Saparov, S. Bobev, A. Ozbay, E.R. Nowak, J. Solid State Chem. 181 (2008) 2690–2696.
[25] S.Q. Xia, S. Bobev, Inorg. Chem. 47 (2008) 1919–1921.
[26] B. Saparov, S.Q. Xia, S. Bobev, Inorg. Chem. 47 (2008) 11237–11244.
[27] S.Q. Xia, S. Bobev, J. Am. Chem. Soc. 129 (2007) 4049–4057.
[28] U. Von Barth, L. Hedin, J. Phys. C 5 (1972) 1629–1642.
[29] J. Singh, Optical Properties of Condensed Matter and Applications, John Wiley & Sons, England, ISBN-13 978-0-470-02192-7 (HB), 2006.
[30] S. Gao, Comput. Phys. Commun. 153 (2003) 190–198.
[31] K. Schwarz, J. Solid State Chem. 176 (2003) 319–328.

[32] P. Balaha, K. Shewartz, G.K.H. Madsen, D. Kvsnicka, J. Luitz, WIEN2K, An Augmented Plane Wave + Local Orbitals Program for Calculating Crystals Properties, Karlheinz Schewartz, Techn. Universitat, Wien, Austria, ISBN 3-9501031-1-2, 2001.
[33] D.M. Ceperley, B.I. Alder, Phys. Rev. Lett. 45 (1980) 566–569.
[34] J.P. Perdew, K. Burke, M. Ernzerhof, Phys. Rev. Lett. 77 (1996) 3865–3868.
[35] E. Engel, S.H. Voskov, Phys. Rev. B 47 (1993) 13164–13174.
[36] Z. Charifi, H. Baaziz, A.H. Reshak, Phys. Status Solidi (b) 244 (2007) 3154–3167.
[37] A.H. Reshak, Z. Charifi, H. Baaziz, Eur. Phys. J. B. 60 (2007) 463–468.
[38] A.H. Reshak, S.A. Khan, Compos. Mater. Sci. 78 (2013) 91–97.
[39] R. Hoffman, Rev. Mod. Phys. 60 (1988) 601–628.
[40] C.D. Gellatt, A.R. Willaims, V.L. Moruzzi, Phys. Rev. B 27 (1983) 2005–2013.
[41] S.A. Khan, A.H. Reshak, Int. J. Electrochem. Sci. 8 (2013) 9459–9473.
[42] A. Delin, P. Ravindran, O. Eriksson, J.M. Wills, Int. J. Quantum Chem. 69 (1998) 349–358.
[43] H. Tributsch, A. Naturforsch. 32A (1977) 972.
[44] A.H. Reshak, Xuean Chen, S. Auluck, I.V. Kityk, J. Chem. Phys. 129 (2008) 204111–204118.
[45] M.S. Dresselhaus, Solid State Physics Part 11, Opt. Prop. Solids (2001).
[46] D.R. Penn, Phys. Rev. B. 128 (1962) 2093–2097.
[47] L. Marton, Rev. Mod. Phys. 28 (1956) 172–184.
[48] K.C. Barron, Thesis for Bachelor degree Submitted to Department of Mechanical Engineering Massachusetts Institute of Technology (MIT), 2005.
[49] G.K.H. Madsen, D.J. Singh, Comput. Phys. Commun. 175 (2006) 67–71.
[50] P. Hua, W. Chun Lei, L. Ji Chao, Z. Rui-Zhi, W. Hong Chao, S. Yi, Chin. Phys. B. 20 No. 4 (2011) 0461031–0461035.
[51] D. Wang, L. Tang, M.Q. Long, Z.G. Shuai, J. Chem. Phys. 131 (2009) 224704–224709.
[52] J.M. Clemens Lasance, Issue: November 2006. <http://www.electronics-cooling.com/2006/11/the-seebeck-coefficient/>.
[53] D. Vashaee, A. Shakouri, J. Appl. Phys. 95 (2004) 1233–1245.
[54] M.I. Kolinko, I.V. Kityk, A.S. Krochuk, J. Phys. Chem. Solids. 53 (1992) 1315–1320.
[55] J. Li, J. Sui, Y. Pei, C. Barreteau, D. Berardan, N. Dragoe, W. Cai, J. He, L. Zhao, Energy Environ. Sci. 5 (2012) 8543–8547.